Transp Porous Med (2015) 108:85–104
DOI 10.1007/s11242-015-0474-0

Laboratory and Numerical Studies of Heat Extraction from Hot Porous Media by Means of Supercritical CO_2

Mario J. Magliocco · Steven D. Glaser · Timothy J. Kneafsey

Received: 16 April 2013 / Accepted: 10 February 2015 / Published online: 18 February 2015

Abstract The use of CO_2 as a heat transfer fluid has been proposed as an alternative to water in enhanced geothermal systems (EGS) and in CO_2-plume geothermal systems (CPG). Numerical simulations have shown that under expected EGS operating conditions, CO_2 would achieve more efficient heat extraction performance compared to water, especially at sites with low geothermal temperatures and low subsurface heat flow rates. With increased interest in carbon capture and sequestration (CCS), the possibility of combining geothermal energy production with carbon sequestration is actively being explored. Simulations have shown that CO_2-based geothermal energy production could substantially offset the cost of CCS. Since numerical models are critical for the planning and operation of geothermal systems that employ CO_2 as the working fluid, it is important to validate the results of the current numerical tools against real- world experimental data. In a set of laboratory experiments, we have investigated heat extraction by flowing dry supercritical CO_2 through a heated porous medium in a laboratory pressure vessel and have compared experimental results with a numerical model using TOUGH2 with the ECO2N module. In addition, experiments were performed using (1) CO_2 and (2) water as the working fluids under similar operating conditions in order to compare the heat transfer behavior and the overall heat extraction rates. Our laboratory apparatus is capable of operating at temperatures up to 200 °C, pressures up to 34.5 MPa, and flow rates up to 400 ml/min. The experimental system was designed such that measurements and controls at the boundaries could be readily modeled using TOUGH2. We have made estimates of the density and the effective thermal conductivity of our saturated porous media, and have found that both properties change significantly during the course of experiments. The large changes in CO_2 density, due to decreasing system temperatures, can result in fluid accumulation in the system that may have significant impacts on geothermal reservoir management. The large changes in thermal conductivity as a function of temperature

M. J. Magliocco (✉) · S. D. Glaser
Department Civil and Environmental Engineering, University of California, Berkeley, CA 94720, USA
e-mail: mag@berkeley.edu

T. J. Kneafsey
Lawrence Berkeley National Laboratory, Berkeley, CA 94720, USA

are of concern because the TOUGH2 code does not update the thermal conductivity of the system during the course of a simulation. Our data can be used by geologic reservoir modelers to ensure that their models accurately capture the heat extraction behavior of CO_2 to aid in the further investigations of EGS, CPG, and CCS.

Keywords Carbon dioxide · Heat transfer · Laboratory experiment · Numerical simulation · Enhanced (engineered) geothermal systems

1 Introduction

Geothermal energy is a vast resource that, if efficiently utilized, could contribute significantly toward meeting the base load energy demand in the USA (Tester et al. 2006). Traditional commercial geothermal electricity production is dependent on a number of factors including an optimized combination of geological conditions such as presence of hydrothermal fluid, high heat flux, high rock permeability, and/or high rock porosity. Enhanced (or engineered) geothermal systems (EGS) are an attempt to exploit geothermal energy in locations where these conditions are not optimal (Tester et al. 2006). Most EGS strategies involve reservoir stimulation to overcome the lack of porosity and/or permeability of the rock using various chemical and physical processes, as well as supplying the needed heat transfer process fluid (e.g. water or CO_2) (Majer et al. 2007).

The novel concept of using supercritical CO_2 as the working fluid in EGS for both reservoir creation and heat extraction was first proposed by Brown (2000). Subsequent work includes numerical simulations of a five-spot well pattern in a hot dry rock (HDR) system, which estimated an approximately 50 % greater heat extraction rate using CO_2 instead of water given the same operating conditions (Pruess 2006). The advantages of using CO_2 over water as the process fluid in a closed-loop HDR system include (1) much lower viscosity of CO_2 means that substantially larger mass flow rates can be achieved for a given pressure drop between injection and production points, and (2) much larger density difference between cold fluid in the injection well and hot fluid in the producer results in increased buoyancy forces for CO_2, which could reduce or even eliminate pumping requirements. As an ancillary benefit, practical operation of a CO_2-based system would result in de facto carbon sequestration due to the amount of CO_2 required and fluid loss to the surrounding formations (Brown 2000; Pruess 2006).

Currently the large-scale use of CO_2 for EGS energy production is impractical due to the cost of capturing, pressurizing, and transporting CO_2 (Eastman et al. 2013), as well as concerns of induced seismicity from the injections (Majer et al. 2007). If environmentally driven public policy changes require the capture and sequestration of CO_2 on a significant scale, it could be possible to produce geothermal energy at the sequestration site to generate electricity or to simply offset the costs of sequestration (Randolph and Saar 2011).

To avoid concerns of induced seismicity due to hydraulic fracturing, a new concept was developed in which CO_2 is used as a working fluid in geologic reservoirs with high porosity, high permeability, and an overlying low-permeability cap rock (Randolph and Saar 2011). This strategy has been named CO_2-plume geothermal (CPG) in order to differentiate it from conventional EGS systems that may make use of a fracturing stage of reservoir development. In light of the promising modeling results and continued interest in CO_2-based geothermal energy production, it is necessary to validate the theoretical tools with practical laboratory and field experiments.

This paper presents the design, implementation, and results of a laboratory-scale CO_2-based heat extraction experiment with the goals of producing a data set that can be compared to results of reservoir numerical modeling tools at the tested conditions, exploring the heat transfer behavior of the system under various operating conditions, and comparing the performance of CO_2- and water-based systems operated under the same conditions. TOUGH2/ECO2N (Pruess 2004; Pruess and Spycher 2007) was the modeling tool we selected because the ECO2N module has incorporated CO_2 properties up to temperatures of 110 °C and pressures up to 60 MPa.

2 Experiment Description

Our research consisted of two major efforts: the creation of laboratory-derived data sets of heat transfer in geologic media using supercritical CO_2, and the creation of a well-behaved numerical model of the physical experiment evaluated using TOUGH2 and ECO2N. For these experiments, we injected temperature-controlled CO_2 under specified conditions into a large heated, sand-filled pressure vessel, and measured temperatures at 23 locations within the sample. We also measured the mass rate of fluid injection, injection pressure, vessel outlet pressure, and the pressure difference between the injection and outlet ports of the vessel.

2.1 Experimental Apparatus

The apparatus consists of a temperature-controlled pressure vessel filled with a porous medium through which temperature-controlled fluid could be introduced by means of high-pressure, high-flow rate pumps (Fig. 1). The pumps could be operated to provide a constant fluid injection rate, or a constant differential pressure. The fluid was delivered by a pair of Quizix C-6000-5K pumps, capable of 34.5 MPa and 400 ml/min fluid delivery rate. The pumps

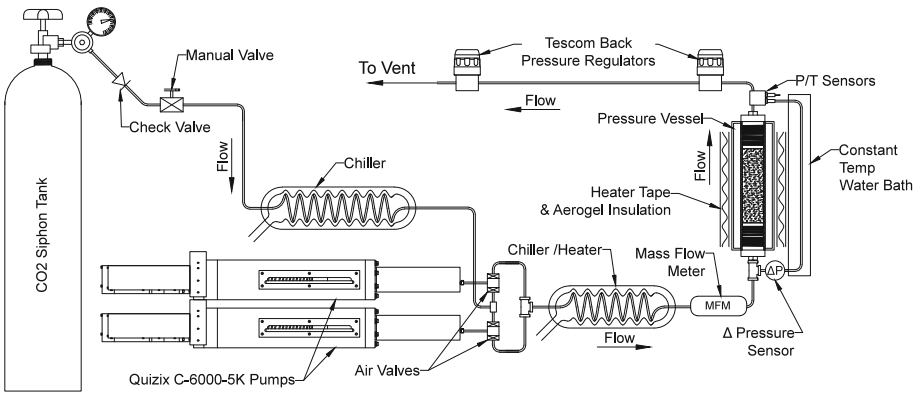

Fig. 1 Diagram of experimental apparatus. Fluid was supplied by a siphon style CO_2 tank. Fluid was driven by a pair of pumps and fed through air-actuated valves. The fluid was then either chilled or heated before it passed through a mass flow meter and into the bottom inlet of the cylindrical pressure vessel that was oriented vertically. A differential pressure sensor was connected hydraulically to the inlet and outlet of the vessel via a temperature-controlled length of tubing that was also oriented vertically. Pressure and temperature sensors were located at the outlet (*top*) of the vessel. Pressure in the fluid exiting the vessel was reduced by a pair of feedback-controlled backpressure regulators, which released the fluid to the atmosphere. The vessel was packed with sand and wrapped in heater tape, which was subsequently covered by a fitted aerogel insulation blanket

can precisely control continuous and pulse-free flow with a resolution of 27.2 nanoliters. To ensure that the pumps were filled with high-density liquid CO_2, the injection fluid was passed through a chiller before entering the pumps. The temperature of the fluid leaving the pumps was chilled or heated depending on the desired experimental parameters. To quantify the mass of CO_2 entering the sample, the injection fluid passes through a Siemens Sitrans MASS 2100-D3 coriolis-style mass flow meter before entering the vessel.

The pressure vessel (High Pressure Equipment Company TOC 31-20) was a hollow type 304 stainless steel cylinder with an inside diameter of 9.1 cm, outside diameter of 12.7, 50.8 cm distance between the type 316 stainless steel end caps secured by 4430 alloy steel caps. The vessel has a pressure safety rating of 34.5 MPa (345 bar, 5000 psi). Instrumentation and flow access to the interior of the vessel are through three axial passages through one end cap (typically the bottom end cap), and one passage through the other (top). The central passages through the end caps were used as the injection and production ports, and the remaining two passages were used exclusively to pass thermocouples through. The vessel was oriented vertically since it has been shown that even for small-length scales, buoyant effects of CO_2 can have a large effect on the dynamics of a CO_2-based system (Liao and Zhao 2002). For a horizontal flow arrangement, buoyant forces can result in pressure gradients that are oriented perpendicular to the vessel axis, complicating the dynamics and test evaluation. For modeling and comparison purposes, the experiments were operated vertically such that the flow path was in the same orientation as the gravity-induced pressure gradient.

Temperature measurements within the sample were made with 23 stainless steel clad type-T thermocouples, which have a small diameter (0.79mm) in order to increase the sensor response time and to minimize disturbance to fluid flow. The thermocouples were arranged at various elevations and radii in the sample such that each successive vertical level was offset angularly to minimize vertical sensor shadowing (Fig. 2; Table 1). The offset angle we used was based on the "Golden Angle" (137.5°), found in plant phyllotaxis that has been shown to minimize shadowing (King et al. 2004). At one elevation in the porous media, two thermocouples were mirrored so that they were both at the same radial distance from the central axis of the vessel to test our assumption of a radial symmetry in the heat transfer process. An Agilent digital multimeter connected to a computer recorded the thermocouple voltages and converted them to temperature.

Because the end caps are massive and heated, the 1/4 inch inner diameter injection port of the vessel was lined with a length of 1/4 inch outer diameter nylon tubing through the end cap in order to provide thermal insulation for the injected fluid as it passed through the end cap. The injection port was also fitted with a single thermocouple, mounted where the injected fluid enters the sample space to measure the temperature of the CO_2 as it entered.

The sand used in the test sample was prepared from F95 Ottawa silica sand (US Silica). Sieving and washing resulted in a narrow grain- size distribution (Fig. 3). The mean grain size falls between 105 and 147 microns with no measurable portion below a grain size of 45 microns.

The sand was dry-placed in the vessel in multiple lifts with vibratory compaction between lifts. This method produced a relative density of 84 percent. The porous sample properties are listed in Table 2. Quartz crystal is highly anisotropic, and the thermal conductivity can vary greatly depending on the direction of the crystal axis (Powell et al. 1966). The value we used for the solid sand grains is based on a random distribution of crystal axis orientations using the arithmetic mean as calculated by Woodside and Messmer (1961).

The vessel was wrapped with five eight-foot lengths of fiberglass fabric covered heat tape that extended around the exterior of the cylinder and both end caps, with an output of 1248 Watts each for a total possible output of 6240 W. The heat tape thermal output was

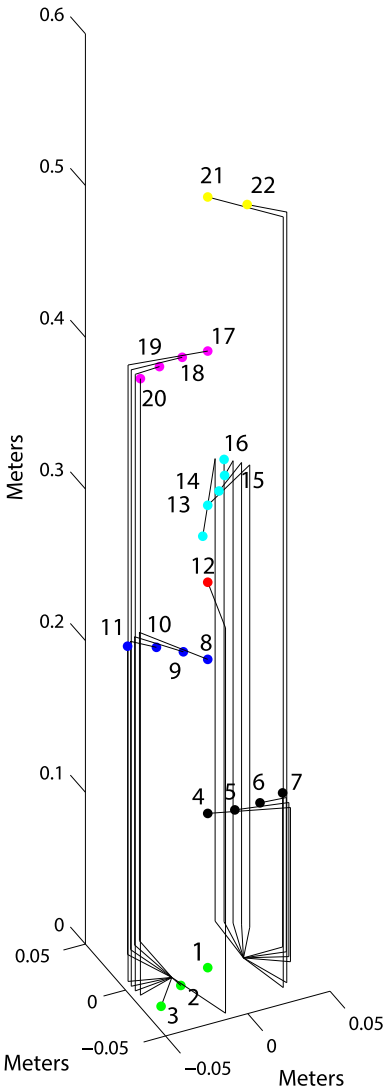

Fig. 2 Orthographic diagram of thermocouple placement inside the vessel. Axis units are in meters

regulated by a closed-loop controller that used the feedback from a single thermocouple secured on the vessel exterior to approximate a constant temperature boundary based on a set point. Finally the vessel was wrapped in an aerogel insulation jacket and sealed. The aerogel insulation jacket was constructed with a 5 mm thick internal layer of silica aerogel (20–23 mW/m/K thermal conductivity) reinforced with a non-woven, glass-fiber batting, which was then covered with a reflective Teflon material.

The pressure at the outlet of the vessel was controlled by a pair of digital backpressure regulators arranged in series. The fluid exiting the backpressure regulators was vented to the atmosphere. A differential pressure sensor was located at the base of the vessel and hydraulically connected to the inlet and outlet of the vessel by means of 1/8th inch stainless steel tubing. The vertically oriented length of tubing that connected the differential pressure

Table 1 Location and numbering of thermocouples

Thermocouple	Elevation (cm)	Radius (cm)
1	0	0
2	0	2.3
3	0	4.6
4	10.2	0
5	10.2	1.5
6	10.2	3.0
7	10.2	4.6
8	20.3	0
9	20.3	1.5
10	20.3	3.0
11	20.3	4.6
12	25.4	0
13	30.5	0
14	30.5	1.5
15	30.5	3.0
16	30.5	4.6
17	40.6	0
18	40.6	1.5
19	40.6	3.0
20	40.6	4.6
21	50.8	0
22	50.8	2.3

This table excludes the thermocouple that duplicates the radial position of number 15

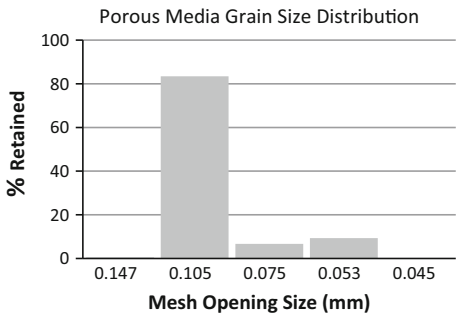

Fig. 3 Grain-size distribution of sorted Ottawa sand

sensor to the inlet was encased in a constant temperature water bath. It was found in early tests, before the connecting tubing was encased in a bath, that the small variations in fluid temperature in this section of tubing resulted in large variations in fluid density that significantly impacted the differential pressure reading. The constant temperature bath was then added to impose a temperature on the fluid that hydraulically connects the outlet of the vessel with the differential pressure transducer that was located below at the inlet of the vessel. This temperature was measured throughout the experiment but was kept at a nominal temperature of 10 °C by means of a laboratory water chiller/circulator. Since the outlet pressure was specified and controlled by backpressure regulators, was held constant throughout the

Table 2 Design case system properties

Porous core properties	
Total core length	$L = 50.8\,\text{cm}$
Cross-sectional area	$A = 6.54 \times 10^{-3}\ \text{m}^2$
Crystalline quartz density	$\rho_R = 2650\ \text{kg/m}^3$
Crystalline quartz-specific heat	$C_R = 830\ \text{J/kg/K}$
Crystalline quartz thermal conductivity	$K = 8\,\text{W/m/K}$
CO_2 saturated sand effective thermal conductivity range	0.22–1.0 W/m/K
Permeability	$k = 9.3 \times 10^{-13}\ \text{m}^2$
Porosity	$\phi = 41\,\%$
Mean grain size d_{50}	$d_{50} \approx 0.105$ mm

experimental runs (within a few thousand Pascals except at flow initiation), and the water bath temperature was held constant (within a few degrees of 10 °C), the weight of the fluid in the connecting tubing was also relatively constant and therefore did not significantly affect the differential pressure reading. The outlet pressure and the water bath temperature were measured during the experiment so that any variations were recorded and could be used to calculate any changes in the density of the fluid in the tubing and then be used to correct the differential pressure reading if needed. The short section of tubing that hydraulically connected the differential pressure sensor to the inlet was not incased in a water bath since it was oriented horizontally. The constant temperature bath around the differential pressure connection tubing would not be necessary when water was employed as a working fluid as water does not significantly change density with changes in pressure and temperature at the scale of our experiment.

We developed software that incorporates experimental control and data acquisition. All sensor readings were collected by a single LabVIEW-based program that allows for accurate time synchronization of experimental data. The program was capable of controlling the pumps and the backpressure regulators. Combining these functions allowed for a tightly integrated experimental setup, faster data processing, faster experimental turnaround time, and reduced experimental errors.

2.2 Experiment Procedure

At the experiment initiation, the sand-packed vessel was filled with CO_2 and pressurized to the experiment pressure, and the vessel was heated to the desired initial temperature. The pumps and tubing were then filled with CO_2 and pressurized to the vessel pressure. The backpressure regulators were set to the desired outlet pressure, the heater tape was turned off, and CO_2 at the specified temperature and pressure was injected into the bottom of the vessel at a prescribed volumetric flow rate. The pumps were operated in an alternating order, and while one pump was injecting fluid into the sample, the other pump would refill. Multiple pump volumes were used in the experiments, which were terminated as the system approached equilibrium. The temperature of the injected fluid was controlled by the laboratory water chiller/circulator that pumped water through the pump water jackets and the water bath heat exchanger located before the vessel inlet. The laboratory water chiller was set for a nominal temperature of 10 °C. The actual injection temperature was measured by a thermocouple located at the inlet of the sample. All thermocouple readings were collected at a frequency of 10 samples per minute.

2.3 Modeling

A 2-D axisymmetric model of the sample and experimental apparatus was implemented in TOUGH2/ECO2N (Pruess 2007, 2004) and included the porous medium, steel vessel, and inlet and outlet material domains. The majority of the modeling work was executed on a dual core 64-bit x86 processor running Apple OSX operating system. A suite of MATLAB scripts was written to allow automatic generation of the mesh file, input files, and extraction and plotting of the postsimulation data. A mesh generation script allowed properly sized models to be produced rapidly with user-selectable quantity of cells in each domain axis. For the modeling results shown in this paper, a resolution of 44 layers in the vertical direction and seven annuli in the radial direction was used with the same dimensions as the actual experimental apparatus. A cell was set as a mass flow rate source for the injection point of the model. The outlet of the vessel was modeled as a time-independent Dirichlet boundary by use of an "inactive" cell (Pruess 2004). The exterior of the vessel, excluding the inlet and outlet, was treated as a no-flux boundary by omitting any flow connections across the surface. The initial conditions such as the initial temperature distribution were generated by a MATLAB script that analyzed the data from the experimental run being modeled.

3 Results and Discussion

3.1 Experimental Results

Sixteen single-phase CO_2 experiments were performed under a variety of conditions using slightly different versions of the experimental apparatus. We also performed an experiment with single-phase water, and an experiment in which we injected CO_2 into a water-saturated core. Here we present data for three representative single-phase CO_2 experiments operated under three different parameters listed in Table 2. The temperature data from the twenty-two (ignoring the redundant thermocouple) thermocouples from a typical experimental run is shown in Fig. 4. The thermocouples are numbered primarily in order of increasing radii and secondarily by increasing elevation in the vessel. Thermocouple 1, for example, is located on the central axis at the bottom of the vessel, while thermocouple number 22 is located near the vessel wall at the top of the vessel (Fig. 2). All temperature history plots in this paper use the same color and line style scheme to indicate the thermocouple location. The plot color indicates the thermocouple elevation (corresponding to colored markers in Fig. 2), and the line style indicates the radial location, going from a solid line at the central axis, followed by dot-dashed, dashed, and finally dotted lines indicating a location at the vessel wall.

In all experiments, there was an initial vertically oriented temperature gradient present in the saturated medium with a lower temperature at the base of the vessel. Upon introduction of the cold CO_2 at the sample bottom, a temperature front developed. The temperature front can be seen as a downward trend in Fig. 4 as it passes axially through the sample past the measurement locations. The initial sharp temperature drop that begins at time $t = 0$ in the plot for Thermocouple 1 at the injection port (green solid curve) occurred at the same time that the pump outlet valve was opened before injection was initiated and likely resulted in a small amount of cold injection fluid entering the vessel. The subsequent spike in temperature (approximately 17 °C) seen at the inlet (solid green line) is likely due to the passage of a hot slug of CO_2 that became heated as it rested in the tubing that passed through the end cap before injection began and after the pump valves were opened. There was also a very small transient increase in temperature (approximately 0.3 °C) at the other thermocouple elevations

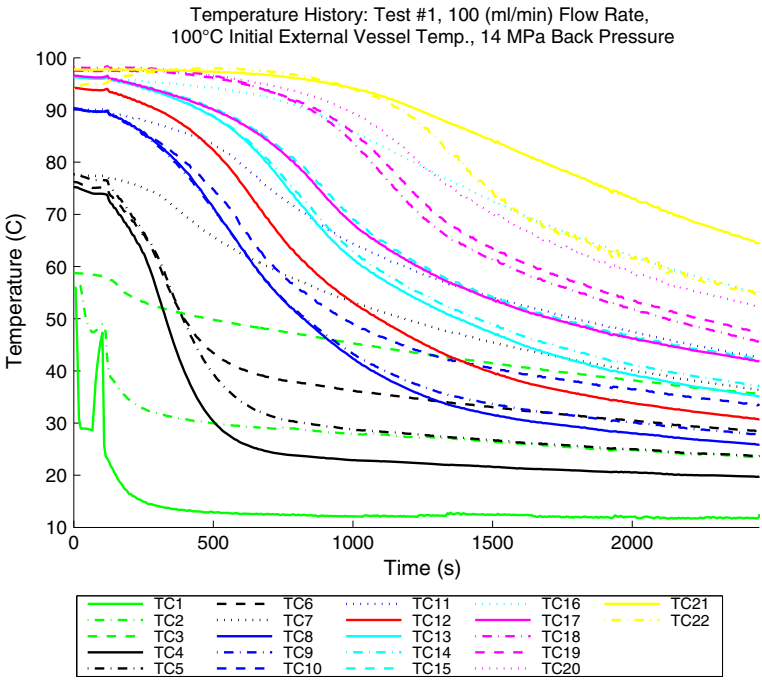

Fig. 4 Temperature versus time data from twenty-two thermocouples from Experiment 1

(TCs 4-22) after the start of injection that is a response to brief increase of pressure in the vessel (approximately 0.48 MPa) due to a small delay in the operation of the backpressure regulator transitioning from the no-flow state.

The temperature fronts as exhibited by the temperature history plot from Experiment 1 (Fig. 4) had a relatively smooth shape and gentle slope when compared with the other experiments that were operated with a higher CO_2 injection rate (discussed below). After injection was initiated, a radial temperature gradient developed, indicated by curves from thermocouples at the same elevation (same color) that began at the same initial temperature and diverged over time. This behavior can be easily seen in the way the blue set of curves (20 cm elevation in the sand pack) diverge in temperature after they were all initially at 90 °C. As the experiment progressed, the more exterior locations (dotted lines) generally trend toward a higher temperature than those more centrally located (solid lines), because of the heat stored in the wall of the steel vessel. This behavior is not seen at the top of the vessel (yellow lines), most likely due to the geometry at the outlet end of the vessel. The initial temperature distribution and developing radial temperature gradients are more apparent in the contour plots of the temperature data. Figure 5 shows the interpolated temperatures for a vertical cross section of the vessel at different times in Experiment 1.

3.2 Thermal Transport

The characteristic rates of the advective and conductive processes can be compared using the dimensionless Peclet number (Pe). The Peclet number can be expressed as the ratio of the time required for both processes to pass across the length scale in question, or conduction time over advection time.

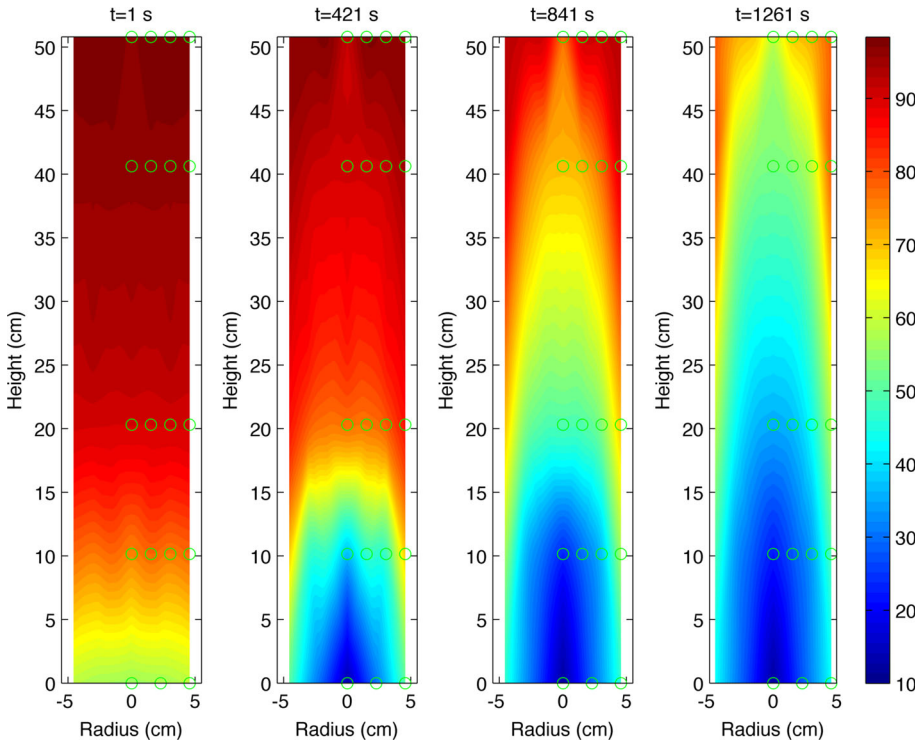

Fig. 5 Interpolated contour plots of the internal temperatures of Experiment 1 at times $t = 1$, 421, 841, and 1,261 s. The CO_2 inlet temperature is shown in Fig. 4. A 2D spline interpolation was used, and the relatively sparse data set resulted in some artifacts; for this reason, the data from the single thermocouple at the elevation of 30 cm (TC 12) were omitted. Thermocouple locations are indicated by *small circles*

$$\mathrm{Pe} = \frac{t_{\mathrm{cond}}}{t_{\mathrm{ad}}} = \frac{L^2 / D_{\mathrm{th}}}{t_{\mathrm{ad}}} = \frac{L^2}{D_{\mathrm{th}} \left(\frac{L}{V_{\mathrm{p}}} \right)} = \frac{L V_{\mathrm{p}}}{D_{\mathrm{th}}} \tag{1}$$

In Eq. (1) t_{cond} is the characteristic thermal conduction time, t_{ad} is the characteristic fluid advection time, D_{th} is the thermal diffusivity, L is the characteristic length, and V_{p} is the pore velocity. This formulation ignores the thermal retardation factor effect on thermal advection and instead compares the bulk stagnant thermal conduction time to the fluid mass advection time. This assumes a null specific heat capacity of the sand for the advection. The bulk pore velocity for the experiment was oriented in the vertical direction as the fluid was pumped into the inlet at the bottom of the vessel and was produced at the outlet at the top of the vessel. Since the flow in the vessel was oriented vertically, all the Peclet numbers calculated and referenced in this paper were for the vertical direction. Heat transfer in the radial direction from the heated stainless steel vessel walls toward center of the sample was largely conductive/dispersive due to the lack of imposed flow in the radial direction.

The bulk stagnant thermal conduction time was found by estimating the thermal diffusivity of the sand and CO_2 at experimental conditions

$$D_{\mathrm{th}} = \frac{\lambda_{\mathrm{eff}}}{\rho_{\mathrm{avg}} C_{\mathrm{p,avg}}} \tag{2}$$

Table 3 Test conditions

Test #	Initial average vessel temperature (°C)	Backpressure (MPa)	Flow rate (ml/min)	Estimated mean initial Pe	Estimated mean final Pe	Estimated mass accumulation (g)
1	86	13.8	100	2.8×10^3	1.1×10^3	652
2	52	8.3	200	1.1×10^4	2.0×10^3	872
3	59	8.3	100	1.2×10^4	1.2×10^3	816

where λ_{eff} is the estimated effective thermal conductivity of the CO_2 -sand matrix, ρ_{avg} is the volumetric average density of the CO_2 sand matrix, and $C_{\text{p,avg}}$ is the average of the specific heat of the CO_2-sand matrix. In order to estimate the effective thermal conductivity of the CO_2-sand matrix, we used an equation from Kunii and Smith (1960) that assumes spherical particles in a packed bed, and neglects radiation and heat conduction through the grain contacts. This equation was found to match well with experimental measurements even at solid to fluid thermal conductivity ratios over 20 (Woodside and Messmer 1961), without the need for finding extensive properties such as grain-contact pressure and area. The estimated effective thermal conductivity of the CO_2-sand matrix, λ_{eff} is

$$\lambda_{\text{eff}} = \lambda_{\text{f}} \left[\phi + \frac{1-\phi}{\varepsilon + \frac{2}{3}\lambda_{\text{f}}/\lambda_{\text{s}}} \right] \tag{3}$$

where λ_{f} is the thermal conductivity of the fluid, λ_{s} is the thermal conductivity of the solid, ϕ is the porosity, and ε is a parameter based on the packing configuration of spherical particles. The parameter ε is found by linearly interpolating between ε_1 which corresponds to a loose packing of spheres ($\phi = 0.476$) and ε_2 which corresponds to a close packing of spheres ($\phi = 0.260$) by means of the equation:

$$\varepsilon = \varepsilon_2 + \frac{(\phi - 0.260)\,(\varepsilon_1 - \varepsilon_2)}{0.217} \tag{4}$$

Kunii and Smith (1960) provide a plot that relates the values of ε_1 and ε_2 to the ratio of solid to fluid thermal conductivities ($\lambda_{\text{s}}/\lambda_{\text{f}}$). The thermal conductivity and all other CO_2 properties used for our calculations outside of TOUGH2 were based upon data from the NIST Standard Reference Database 69 (Lemmon et al. 2010).

Because conditions in our experiment changed over time, the CO_2 density changed as internal vessel temperatures changed, and it was impossible to calculate a single Pe number that was valid for all times and all locations inside the vessel. Instead we calculated a Pe number for the initial and final bulk conditions of the experiments neglecting CO_2 accumulation, which would alter the pore velocity throughout the column. The estimated initial and final Peclet numbers are shown in Table 3.

The interplay between advective and conductive transport is also demonstrated by the shape of the temperature versus time curves. An almost purely advective dominated process would feature sharp thermal fronts, a near vertical slope at the time when the cold fluid slug reached the thermocouple, and would have a higher Pe number. A conductive dominated process would exhibit a gentle slope with smooth transitions and would correspond to a lower Pe number. For Experiment 1 (Figs. 4, 5 above), the estimated Pe number for the initial condition was 2.8×10^3 and the estimated Pe number for the final condition was 1.1×10^3. Experiment 2 (Figs. 6, 7), which was operated at twice the flow rate of Experiment 1, exhibits a

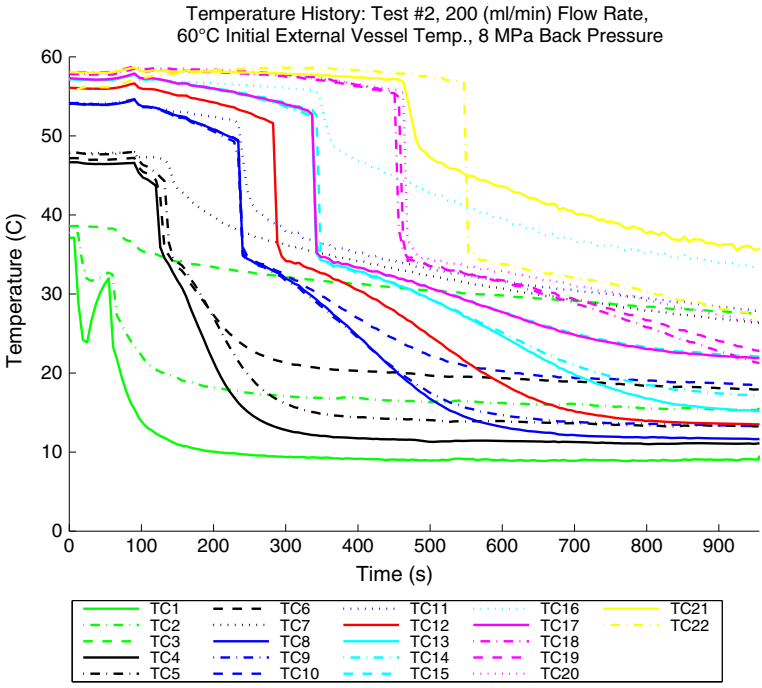

Fig. 6 Temperature versus time data from twenty-two thermocouples from Experiment 2

much more steeply sloped temperature front that, along with the higher estimated Pe numbers (1.1×10^4 initial -2.8×10^3 final), indicates that the heat transfer process was advectively dominated. The temperature fronts for Experiment 3 (Fig. 8), which was operated at a lower back pressure and initial temperature than Experiment 1, are also relatively steep indicating an advectively dominated process which corresponds with the calculated Pe numbers (1.2×10^4–1.2×10^3).

3.3 CO_2 Accumulation

Two methods were used to measure the mass flow rate at the inlet of the vessel: the lookup method and the mass flow rate meter. The lookup method used the volumetric flow rate of the pump, the temperature and pressure of the fluid exiting the pumps, and a density lookup table for CO_2 (Lemmon et al. 2010) in order to estimate the mass flow rate delivered. The lookup method for determining mass flow delivered to the vessel from the pump corresponded well with the data from the mass flow meter at the injection side of the vessel. CO_2 accumulation was found to be significant as the temperature of the fluid in the vessel decreased. In Experiment 1, the mean initial vessel temperature of 87 °C and initial pressure of 13.8 MPa correspond to a CO_2 density of 341 kg/m^3; at the end of the experimental run ($t = 2350$ s), the mean vessel temperature was 33 °C which at 13.8 MPa corresponds to a CO_2 density of 814 kg/m^3. This change of temperature results in an approximate density increase of 2.4 times, or an accumulation of 652 g of CO_2 in the pore space. The estimated accumulation of CO_2 in the vessel for all of the experiments can be found in Table 3.

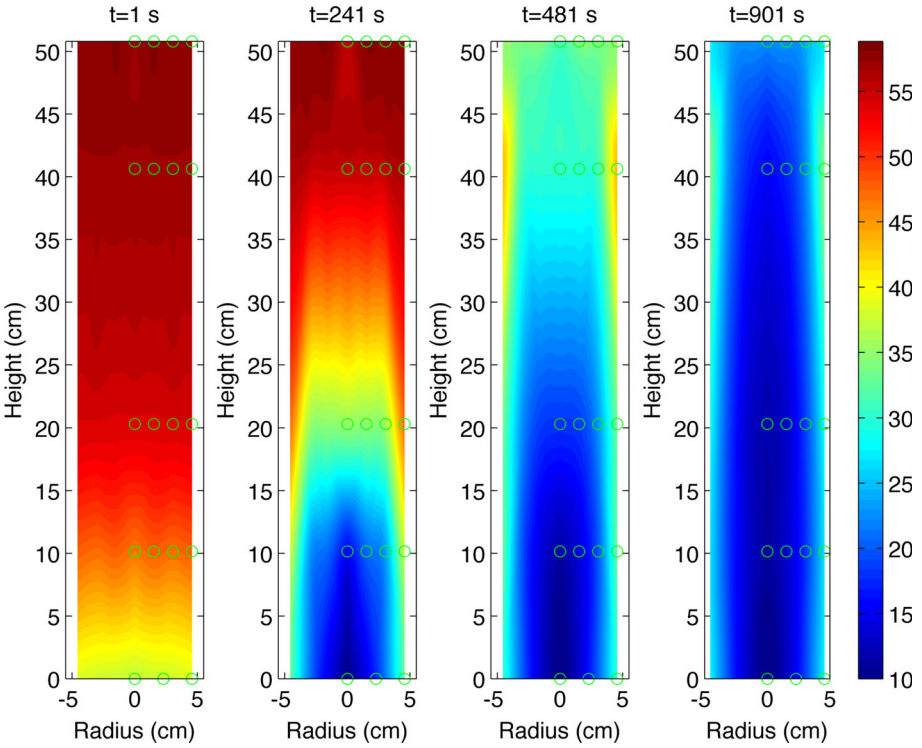

Fig. 7 Interpolated contour plots of the internal temperatures of Experiment 2 at times $t = 1$, 241, 481, and 901 s. Thermocouple locations are indicated by small circles

3.4 CO_2 Versus Water

To compare the performance of CO_2 heat extraction with that of water, we performed a single-phase water run at the same temperature and pressure as a CO_2 run (Fig. 9). Both experiments were performed with an older, less refined version of our apparatus that contained a less dense thermocouple array. To compare the two working fluids, we used a volumetric fluid injection rate of 150 ml/min, an initial sample temperature of 75 °C, and a backpressure of approximately 10 MPa. The CO_2 and water experiments had approximately the same pressure differential across the sample for both water and CO_2 (0.2 MPa), and a similar mass flow rate (2.51 g/s for water, and a range of 2.3–2.04 g/s for CO_2), which allowed a more straightforward comparison of the performance of the two fluids. The injected water and CO_2 increased in temperature after the first two pump volumes because in these earlier tests we recycled the injection fluid. The CO_2 plot shows a much steeper temperature front indicating a more advection-dominated flow than the water experiment. This is due to the lower CO_2 fluid thermal conductivity than water under the experimental conditions. During the course of the experiment, the pore velocity, specific heat, and density of the two fluids were relatively similar, but the thermal conductivity of the CO_2 fluid ranged from 0.04 to 0.11 W/m/K while the water had a thermal conductivity range of 0.58–0.66 W/m/K.

We used the experimental data to calculate the heat extraction rates of the two fluids. Figure 10 shows the heat extraction rates of water (blue line) and CO_2 (red line). The heat extraction rate for the water during the 72–420 s time period of the experiment is significantly

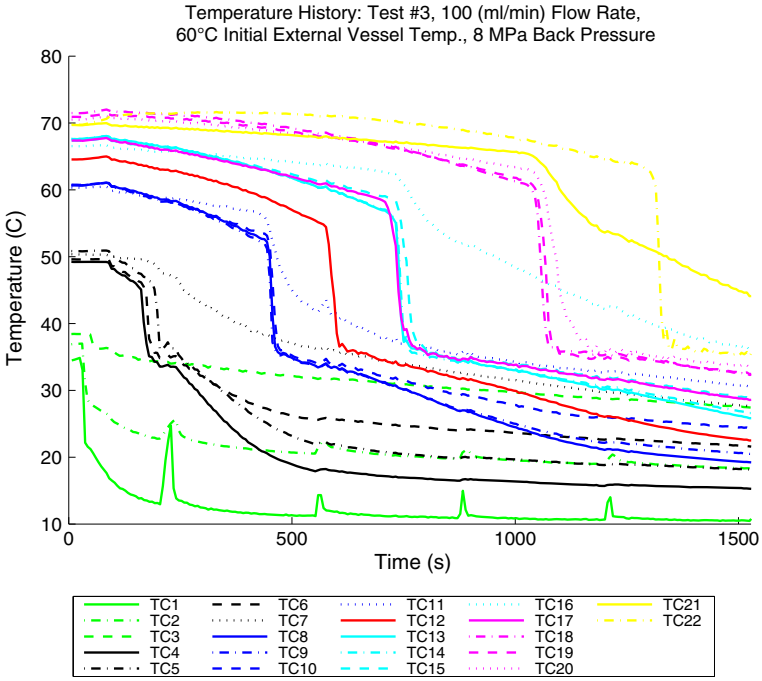

Fig. 8 Temperature versus time data from twenty-two thermocouples from Experiment 3. The impulses at the injection point were due to the selection of a pump mode that did not implement the pulse-free valve operation. There was a slight cessation of flow during pump changeover events that resulted in the fluid in the injection port heating in the steel end cap

higher than that of the CO_2, but the heat extraction rate of the water decreases after the first two pump volumes due to the increased injection temperature. The performance of CO_2 stays somewhat stable despite the fact that the mass flow rate is decreasing during the experiment due to the increase in injection temperature. Since both the water and CO_2 were operated at a similar pressure and volumetric flow rate, it can be assumed that the work performed by the pumps in both experiments was comparable. A complete thermodynamic characterization of the runs would require measurements of the fluid accumulation inside the vessel, which was not recorded for these experiments.

The design of our experiment was primarily intended to produce a data set that could then be used to validate numerical modeling of the use of CO_2 as the working fluid in an EGS reservoir, and was not intended to be directly applicable to full-scale EGS systems. Specifically, our porous medium sample was not designed to replicate the characteristic flow paths that would be expected in a field-scale geothermal system. Despite this, our results can be used to gain insights into the behavior of CO_2 as an EGS working fluid. Our experimental results show that CO_2 and water have comparable behavior under a particular set of initial and operating conditions. This result could be viewed as discouraging in the context of CO_2 based EGS, but was in line with previous modeling results (Pruess 2007). The greater benefits of CO_2 over water are expected to occur in the 5-spot well geometry that is dominated by radial flow due to the differences in the kinematic fluidity of CO_2 as compared to water. The kinematic fluidity can be used to compare the mass flow rate for different fluids within the same porous medium under the same driving pressure differential and is defined as the

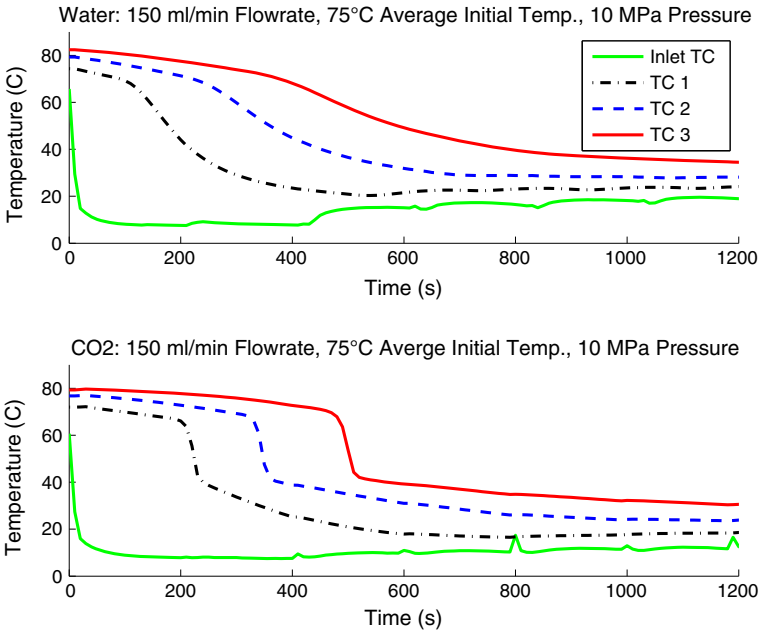

Fig. 9 Comparison of temperature history data of water and CO_2 as working fluids. *Top plot* shows a water run, and the *bottom plot* is a CO_2 run. Data is only shown for centrally located thermocouples. (Thermocouple labeling is not consistent with other figures in this paper due to difference in thermocouple array)

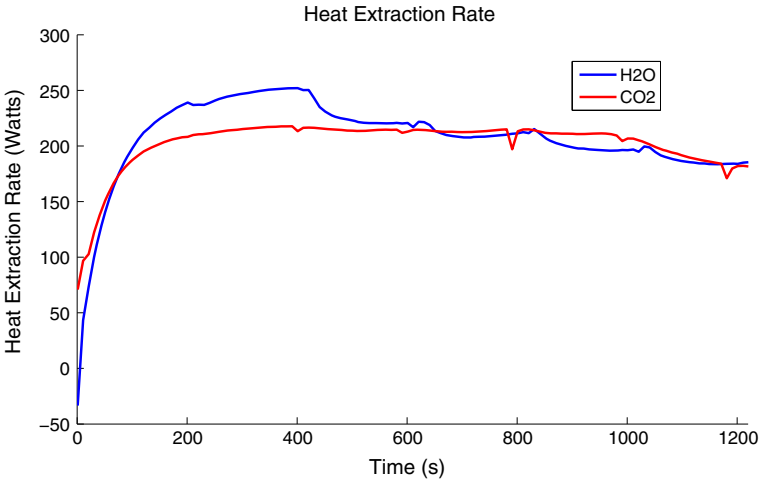

Fig. 10 Comparison of the heat extraction rate of water and CO_2 under similar experimental conditions

reciprocal of the kinematic viscosity, or the ratio between fluid density ρ, and fluid dynamic viscosity μ (kinematic fluidity $= \rho/\mu$).

In a water-based 5-spot EGS system, the majority of the driving head loss occurs near the injection well. This is because the lower kinematic fluidity resulting from the colder conditions coupled with the high Darcy flux due to the radial flow pattern around the well

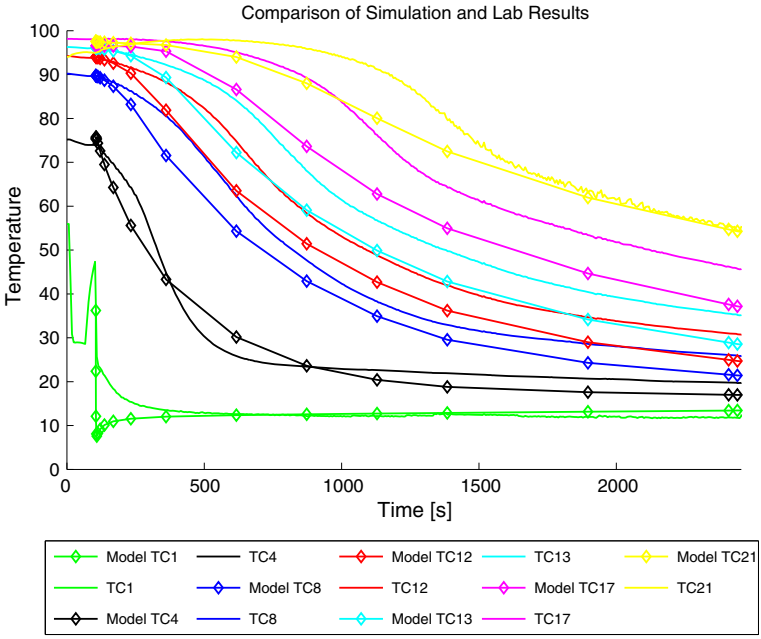

Fig. 11 Experimental and numerical modeling results for Experiment 1. Experimental data are shown by smooth lines and modeled data by *lines* with *markers*

requires a high driving pressure gradient. This is in contrast to the higher kinematic fluidity CO_2-based system where the head loss is much more evenly distributed across the entire flow path. In our apparatus, the flow is predominately linear along the length of the vessel with small portions of radial flow near the inlet and outlet boundaries. In addition, the thermal energy stored in the large end caps used in our vessel may retard the development of cold zones near the fluid injection point.

3.5 Modeling Results

We used custom MATLAB scripts to generate all of the input files for the TOUGH2 simulation. Values for the input data were read directly from recorded data for the experiment being simulated, including mass flow rate, initial temperature distribution, backpressure, injection temperature, and initial effective thermal conductivity of the saturated media. A comparison of simulation and temperature measurements along the central axis of the vessel for Experiment 1 is shown in Fig. 11.

The simulation data are shown with diamond line markers, while the experimental data are shown without markers. It was difficult to achieve a good fit between the experimental data and the simulation output by manually calibrating the simulation variables. There are three possible factors for this behavior: (1) our assumption of perfect insulation, (2) difficulties in exactly replicating the boundary conditions in TOUGH2, and (3) changes in thermal conductivity not updated by TOUGH2. Our assumption of a perfectly insulated vessel boundary could have a minor effect on the data fit but the effect is not in the correct direction (the modeled systems cool faster than the experimental system), but because of the short timescales in our experiments, it is unlikely to have a significant impact. Imperfectly replicating the

boundary conditions may also result in differences, as we have assumed the steel vessel to have a uniform temperature; however, some small nonuniformities were likely as a result of the heat tape arrangement. We believe the most significant factor affecting our ability to fit the model to the experimental data is the manner in which TOUGH2 handles the thermal conductivity of the modeled system.

Heat flux in TOUGH2, conductive and advective, is modeled using the following equation:

$$F_{\text{heat}} = -\lambda \nabla T + \sum h_\beta F_\beta \tag{5}$$

where F_{heat} is the heat flux, λ is the rock formation thermal conductivity under fully liquid saturated conditions, h_β is the specific enthalpy in phase β, and F_β is the advective mass flux of phase β. The value of λ is entered by the user in the TOUGH2 input file and is not updated during the course of the simulation. The assumption that the thermal conductivity of the saturated rock does not change may be valid for relatively incompressible fluids such as water, but it may produce errors for systems where the density of the saturating fluid changes dramatically. For example in Experiment 3, temperatures within the vessel ranged from a minimum temperature of 10.5 °C and a maximum temperature of 72 °C. At operating pressure, this resulted in an estimated effective thermal conductivity that ranged from 0.2 W/(mK) at the highest temperature to a thermal conductivity of 1.0 W/(mK) at the lowest. Depending on the relative importance of conduction in the system, the assumption that thermal conductivity is constant may produce results that differ significantly from the observed data.

To see the effect that the choice of thermal conductivity of the CO_2 saturated sand had on the results of a TOUGH2 simulation, we ran two simulations of Experiment 1 with two different thermal conductivities: 1 W/(mK) and 0.3 W/(mK). The choice of the two thermal conductivities for the simulation was based on the range of estimated effective thermal conductivities calculated from experimental data for that run. The difference of the temperature history results of these two simulations was calculated at the same locations as the experimental thermocouples by subtracting the results of the simulation of the model with a lower thermal conductivity from the results of the model with the higher thermal conductivity, and plotted in Fig. 12.

The differences between the two sets of simulation results using different thermal conductivities was variable with time and space. For example, at locations near the steel vessel wall, the simulation with the higher thermal conductivity resulted in lower temperatures. Conversely, the temperatures closer to the axis of the sample, including the outlet, were higher with a higher thermal conductivity. For this case, a higher thermal conductivity results in higher temperature of the produced fluid throughout the time history of the simulation. The temperature history of the two simulations differed up to 10 °C. The differences in simulation temperature histories that occurred when using different thermal conductivities were within the same order of magnitude as differences we found between our model and experimental results. This exercise was not meant to accurately show the error expected due solely to the TOUGH2 assumption of constant thermal conductivity since that task would require extensive intervention to include updated thermal conductivity in TOUGH2 based on the changing state of the CO_2. These results do illustrate the difficulty that might be encountered in choosing a single thermal conductivity value through either manual or automated calibration techniques. Making the effective thermal conductivity a function of the fluid state would be expected to improve the ability to match the experiment data.

With continued interest in CO_2-based geothermal energy production and the reliance on numerical tools for evaluating its practicality, our results should provide a note of caution for

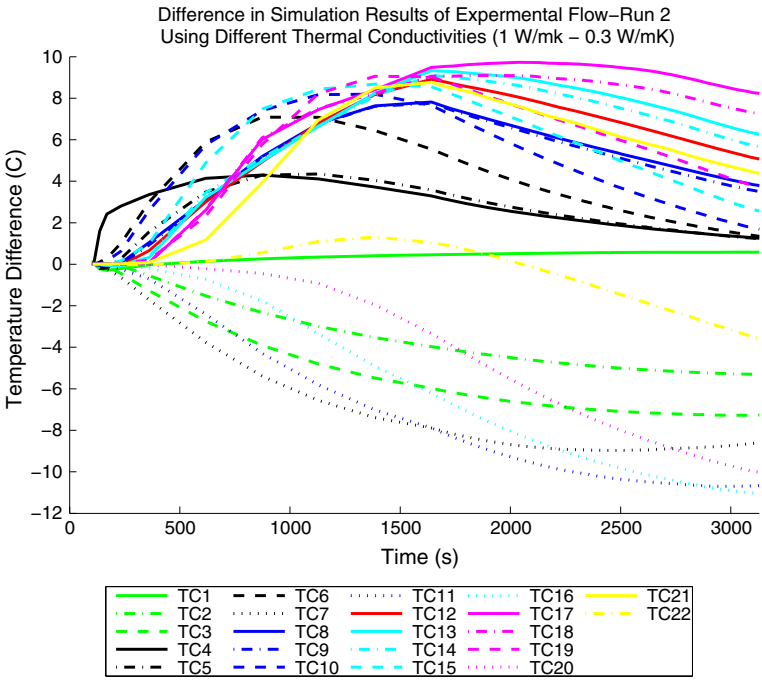

Fig. 12 Difference between simulation results modeled with two different initial thermal conductivities. Results of run at a thermal conductivity of 0.3 W/mK subtracted from the results of a simulation with a thermal conductivity of 1 W/mk

modelers and researchers in this field. A dominant feature of CO_2 as a heat extraction working fluid is the large changes in density that accompany changes in pressure and temperature. While the dynamic density of CO_2 may reduce pumping requirements due to buoyant forces generated as the fluid heats up within the reservoir, the accompanying changes in thermal conductivity should not be ignored when modeling the system. Ignoring changes in thermal conductivity of the CO_2 is not likely to have a large impact on simulations of classical EGS reservoirs that are composed of fractured hot dry rock, since the porosity of these systems is typically low, and the influence of the thermal conductivity of the CO_2 on the effective thermal conductivity of the saturated rock will be small. CPG systems on the other hand are envisioned to be in reservoirs with relatively large porosities on the order of 20 % (Randolph and Saar), where changes in the thermal conductivity of the CO_2 could have a significant impact to the heat flow within the reservoir, and the resulting predicted temperature history of the produced fluid.

Altering the TOUGH2 code to include changes in effective thermal conductivity would be difficult since a simple effective thermal conductivity lookup table based on the temperature and pressure could not be employed in a similar manner to how TOUGH2 handles viscosity and density. This is due to the fact that the effective thermal conductivity is dependent on the ratio of thermal conductivity of the fluid to solid, as well as the packing of the media. It would be possible to create a lookup table of effective thermal conductivities indexed by temperature and pressure using the Konii and Smith model (1960) with our sand pack parameters. Creating such a table and adding the functionality to TOUGH2 and ECO2N would be difficult and would only be applicable to sand packs with the same properties as our sample.

Besides altering the TOUGH2 code, including updated thermal conductivity in the simulation could be accomplished by splitting the mesh up into multiple rock domains with separate entries in the input file. The model could then be run forward with a short simulation time step, the output could be used to make new thermal conductivity estimates, the input file could be updated, and the process repeated for succeeding time steps. The thermal conductivity could be updated by using a method such as that described by Kunii and Smith (1960). Using Eqs. 3 and 4, and the thermal conductivity of the CO_2 (λ_f) given by lookup tables for the temperature and pressure in the region, the λ_{eff} could be computed for each region in order to update the model between time steps. This method would be cumbersome to deploy, but could be used for simulations where it is determined that the changing thermal conductivity contributes significantly to the temperature response of the system.

4 Conclusion

With our experimental apparatus, we were successful at controlling CO_2 injection, vessel backpressure, and measuring temperature changes at many locations within the sample. We have found that the process exhibits significant mass accumulation inside the vessel due to increased CO_2 density as temperatures decreased, as would also be expected in a field implementation of this method contributing to CO_2 sequestration. The large changes in density that are associated with changes in temperature may have important implications for the operation of a field-scale EGS system. For example, the temperatures in a geothermal reservoir would drop as energy is produced from the formation, resulting in CO_2 accumulation. If the energy production is decreased or halted, the reservoir will begin to increase in temperature due to heat flux from the surrounding geological formations, which would then result in an increase in pressure. If this pressure increase is not managed, it could result in unwanted fluid migration or geomechanical impacts (e.g., induced seismicity or ground surface uplift).

The relative importance of the conductive versus advective thermal processes in the direction of flow can be seen in our experimental results and corresponds well to the estimated Peclet numbers. The experiments that exhibited sharper transition and steeper thermal fronts corresponded to a higher estimated Pe range than the experiments that had thermal fronts with gentler slopes and smoother transitions. The performance of water and CO_2 was compared using the same operating conditions, and it was found that the heat extraction performance of each fluid was similar in our linear-flow-dominated vessel. This result was expected and is not applicable to geothermal reservoirs with radial flow patterns.

We constructed a representative model of the system in TOUGH2 using inputs from experimental data, but we were unable to achieve a good fit between experimental data and our simulation results through manual calibration. We believe that more knowledge of the conditions at the vessel boundary could improve our model slightly, but we are more concerned that the TOUGH2 assumption of constant CO_2-sand matrix thermal conductivity can significantly affect the results of the simulation. Estimates of the effective thermal conductivity of our saturated sampled varied by almost an order of magnitude, and this change is not included in the current TOUGH2 code. The differences seen between the experimental results and the simulation results are within the same order of magnitude as seen when different thermal conductivities for the saturated media are chosen for the simulation parameters. We recommend that when modeling a CO_2-based geothermal reservoir with a numerical tool that does not update the effective thermal conductivity during the simulation, users should exercise caution. Using a conceptual model that is suited for the geothermal reservoir structure, the effective thermal conductivity should be estimated for the range of CO_2 densities

that are expected to be encountered in the reservoir operation. The sensitivity of the model should then be tested using the range of effective thermal conductivities, and if results are significantly affected, an alternative modeling method should be found. We are working on expanding our experimental data set to cover more pressures, temperatures, flow rates, and fluid mixtures (CO_2, water, NaCl brine) and hope to publish these data in the near future.

References

Brown, D.W.: A hot dry rock geothermal energy concept utilizing supercritical CO_2 instead of water. In: Proceedings of the Twenty-Fifth Workshop on Geothermal Reservoir Engineering, Stanford University, pp. 233–238 (2000)

Eastman, A.D., Muir, M.P., Energy, G.: CO_2 EGS and the utilization of highly pressurized CO_2 for purposes other than power generation. In: Proceedings of the Twenty-Eighth Workshop on Geothermal Reservoir Engineering. Stanford University (2013)

King, S., Beck, F., Lüttge, U.: On the mystery of the golden angle in phyllotaxis. Plant Cell Environ. **27.6**, 685–695 (2004)

Kunii, D., Smith, J.M.: Heat transfer characteristics of porous rocks. AIChE J. **6**(1), 71–78 (1960)

Lemmon, E.W., McLinden, M.O., Friend, D.G.: Thermophysical properties of fluid systems. NIST chemistry WebBook, NIST standard reference database number 69. In: Linstrom, P.J., Mallard, W.G. (eds.) National Institute of Standards and Technology, Gaithersburg MD, http://webbook.nist.gov, (retrieved September 2010)

Liao, S.M., Zhao, T.S.: Measurements of heat transfer coefficients from supercritical carbon dioxide flowing in horizontal mini/micro channels. J. Heat Transf. **124.3**, 413–420 (2002)

Majer, E.L., Baria, R., Stark, M., Oates, S., Bommer, J., Smith, B., Asanuma, H.: Induced seismicity associated with enhanced geothermal systems. Geothermics **36.3**, 185–222 (2007)

Powell, R.W., Ho, C.Y., Liley, P.E.: Thermal conductivity of selected materials. (No. NSRDS-NBS-8). In: National Standard Reference Data System (1966)

Pruess, K.: The TOUGH codes—a family of simulation tools for multiphase flow and transport processes in permeable media. Vadose Zone J. **3**, 738–746 (2004)

Pruess, K.: Enhanced geothermal systems (EGS) using CO_2 as working fluid—a novel approach for generating renewable energy with simultaneous sequestration of carbon. Geothermics **35**(4), 351–367 (2006)

Pruess, K.: Enhanced geothermal systems (EGS) comparing water with CO_2 as heat transmission fluids. In: Proceedings, New Zealand Geothermal Workshop 2007 Auckland, New Zealand (2007)

Pruess, K., Spycher, N.: ECO2N—a fluid property module for the TOUGH2 code for studies of storage in saline aquifers. Energy Convers. Manag. **48.6**, 1761–1767 (2007)

Randolph, J.B., Saar, M.O.: Coupling carbon dioxide sequestration with geothermal energy capture in naturally permeable, porous geologic formations: implications for CO_2 sequestration. Energy Procedia **4**, 2206–2213 (2011). doi:10.1016/j.egypro.2011.02.108

Tester, J.W., Anderson, B., Batchelor, A., Blackwell, D., DiPippo, R., Drake, E., Garnish, J., Livesay, B., Moore, M.C., Nichols, K., Petty, S., Toksoz, N., Veatch, R., Augustine, C., Baria, R., Murphy, E., Negraru, P., Richards, M.: The future of geothermal energy: impact of enhanced geothermal systems (EGS) on the United States in the 21st century. In: Massachusetts Institute of Technology, DOE Contract DE-AC07-05ID 14517 Final Rept., p. 374 (2006)

Woodside, W.T., Messmer, J.H.: Thermal conductivity of porous media. I. Unconsolidated sands. J. Appl. Phys. **32.9**, 1688–1699 (1961)